J. Mod. Power Syst. Clean Energy (2019) 7(2):254–267
https://doi.org/10.1007/s40565-018-0415-3

Small-signal stability analysis of photovoltaic generation connected to weak AC grid

Qi JIA[1], Gangui YAN[1], Yuru CAI[1], Yonglin LI[1], Jinhao ZHANG[1]

Abstract A small-signal model of photovoltaic (PV) generation connected to weak AC grid is established based on a detailed model of the structure and connection of a PV generation system. An eigenvalue analysis is then employed to study the stability of PV generation for different grid strengths and control parameters in a phase-locked loop (PLL) controller in the voltage source converter. The transfer function of the power control loop in the *dq* rotation frame is developed to reveal the influence mechanism of PLL gains on the small-signal stability of PV generation. The results can be summarized as follows: ① oscillation phenomena at a frequency of about 5 Hz may occur when the grid strength is low; ② the tuning control parameters of the PLL have a noticeable effect on the damping characteristics of the system, and larger proportional gain can improve the system damping;③ within a frequency range of 4-5 Hz, the PLL controller has positive feedback on the power loop of PV generation. A virtual inductance control strategy is proposed to improve the operational stability of PV generation. Finally, a simulation model of PV generation connected to weak AC grid is built in PSCAD/EMTDC and the simulation results are used to validate the analysis.

Keywords Photovoltaic generation, Weak AC grid, Small-signal model, Eigenvalue analysis, Virtual inductance control strategy

1 Introduction

Photovoltaic (PV) generation is an important way to address the environmental challenges of generating electricity from fossil fuels. Due to restricted availability of land and the quality of the solar resource, large-scale PV generation systems in China are mostly located in deserts or semi-deserts where the grid structure is relatively weak, and they are integrated into power systems through voltage source converters (VSCs).

Grid impedance, as an indicator of a weak grid, becomes increasingly important with the increasing capacity of grid-connected PV generation [1, 2]. Output power disturbance of the PV array and grid disturbance will affect the point of common coupling (PCC) voltage and make it unstable. An unstable PCC voltage subsequently affects the dynamics of the VSC control system, and the design of the VSC control system based on the ideal grid conditions is no longer suitable [3, 4]. Therefore, this situation poses challenges to both the control and safe operation of PV generation.

CrossCheck date: 12 March 2018

Electronic supplementary material The online version of this article (https://doi.org/10.1007/s40565-018-0415-3) contains supplementary material, which is available to authorized users.

Received: 4 July 2017 / Accepted: 12 March 2018 / Published online: 20 June 2018

✉ Qi JIA
15948692960@163.com

Gangui YAN
yangg@neepu.edu.cn

Yuru CAI
sxyccyr@163.com

Yonglin LI
liyonglin6633@126.com

Jinhao ZHANG
18686313297@163.com

[1] Northeast Electric Power University, Jilin 132012, China

The stability of PV generation connected to a weak grid has been investigated in several works [5–13]. The authors in [7, 8] proposed an impedance model of a VSC, which was useful for control dynamics and stability studies. Reference [10] established an equivalent VSC that models the *N*-paralleled grid-connected VSCs in PV plants and described the coupling effect due to grid impedance. However, this study ignored the impact of the control strategy. Reference [11] proposed a small-signal model to analyze the stability of DC-link voltage control in the VSC, but it did not consider the impacts of other control loops. References [12, 13] pointed out that the instability phenomenon is related to converter control loops such as the phase-locked loop (PLL) controller and the AC terminal controller.

To avoid instabilities caused by the influence of the weak AC grid, [14] decreased the PLL bandwidth to prevent its interaction with other modes of the system and slow it down, [15] changed the parameters of the AC terminal control loop to speed it up. Although the system remained stable according to these methods, the performance of the VSC was very poor. Reference [16] proposed an artificial bus for VSC synchronization, which was equivalent to reducing the grid impedance. However, the method could not perfectly emulate a physical inductance and it may be sensitive to noise.

In contrast to previous research, this paper proposes a small-signal model of PV generation connected to a weak AC grid. An eigenvalue analysis is employed to study the stability of PV generation for different grid strengths and control parameters in the PLL controller. In order to improve the operational stability of PV generation, a virtual inductance control strategy is proposed based on [16]. The main contributions of this paper are as follows.

1) A thorough analysis of the dynamics of PV generation connected to a weak grid, and the impacts of the controller parameters on the overall system stability.
2) An understanding of the influence mechanism of the PLL control parameters on the small-signal stability of PV generation, based on the transfer function of the power control loops in the *dq* rotation frame.
3) The development of a virtual inductance control strategy to stabilize the performance of PV generation in weak AC grid conditions.

The paper is structured as follows. In Section 2, the configuration of PV generation connected to a weak AC grid is described. Section 3 establishes a small-signal model of PV generation connected to a weak AC grid, including PV array, VSC and grid models. The eigenvalue analysis is presented in Section 4. A virtual inductance control strategy is proposed in Section 5. Section 6 describes case studies of PV generation with the proposed control strategy connected to a weak AC grid. The conclusions are presented in Section 7 to close the paper.

2 Configuration of PV generation connected to weak AC grid

Large-scale PV generation systems are usually far away from load centers and the PV power has to be sent to the main power grid using long distance transmission. When the impedance of the transmission line is significant, the PV generation may be considered to be connected to a weak grid. A simplified but representative model of such a system is shown in Fig. 1 and is used for this study. It has a PV generation system (P_1), a local transmission system (P_2), a long distance transmission system (P_3) and an equivalent circuit of the main grid (P_4).

In Fig. 1, C is the input filter capacitance; U_{dc} is the DC voltage; L_f is the output filter inductance; C_f is the output filter capacitance; R_1 and L_1 are the resistance and inductance of the local transmission system, respectively; R_2 and L_2 are the resistance and inductance of the long distance transmission system; R_g and X_g are the equivalent resistance and equivalent reactance of the grid; U_t and θ_t are the PCC voltage and its phase; Z_g is the grid impedance; and U_g is the grid voltage. In order to simplify the analysis, the above parameters are referred to the output side voltage level of the VSC.

In Fig. 1, the strength of the AC system is generally described by a short-circuit ratio (SCR), as defined in (1). The AC system is regarded as a weak grid when the R_{SCR} is lower than 3. From (1), it can be found that the R_{SCR} decreases with increasing grid impedance.

$$R_{\mathrm{SCR}} = \frac{S_{ac}}{S_{\mathrm{N}}} = \frac{U_g^2}{Z_g S_{\mathrm{N}}} \tag{1}$$

where S_{ac} is the short-circuit capacity of the AC system; S_{N} is the rated power of the PV generation.

In order to simplify the stability analysis of PV generation connected to a weak AC grid, the following assumptions are made:

1) The effect of the output filter capacitor C_f is neglected. The AC capacitor in the VSC is responsible for

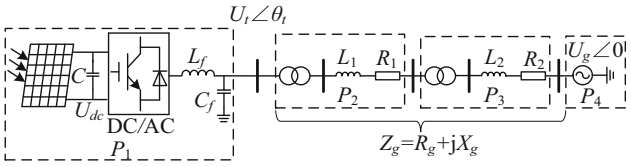

Fig. 1 Configuration of PV generation connected to a weak AC grid

filtering high-frequency harmonics, and this paper focuses on the low-frequency band.

2) The effect of the grid resistance R_g is neglected. The resistance of the grid is smaller than the inductance.
3) The system is lossless apart from the impact of the resistances included in the model in Fig. 1.

3 Modeling of PV generation connected to weak AC grid

3.1 PV array model

Figure 2 shows the configuration of the PV array, where N_p and N_s are the number of parallel and series connected cells, respectively, and I_{PV} is the DC current. The *U-I* characteristic of a PV cell is given by (2), which can be obtained from the manufacturer.

$$I_o = I_{sc}\left[1 - C_1\left(\mathrm{e}^{\frac{U_{dc}}{C_2 U_{oc}}} - 1\right)\right] \tag{2}$$

where I_{sc} is the short-circuit current; U_{oc} is the open-circuit voltage; C_1 and C_2 are given by (3) and (4).

$$C_1 = \left(1 - \frac{I_m}{I_{sc}}\right)\mathrm{e}^{-\frac{U_m}{C_2 U_{oc}}} \tag{3}$$

$$C_2 = \left(\frac{U_m}{U_{oc}} - 1\right) \Big/ \ln\left(1 - \frac{I_m}{I_{sc}}\right) \tag{4}$$

where I_m is the maximum power point current; U_m is the maximum power point voltage. These four parameters are provided by the PV array manufacturer, they can be modified according to (5) when the external conditions change.

$$\begin{cases} I_{sc} = I_{sc,\mathrm{ref}}\dfrac{S}{S_{\mathrm{ref}}}(1 + a\Delta T) \\ U_{oc} = U_{oc,\mathrm{ref}}\ln(e + b\Delta S)(1 - c\Delta T) \\ I_m = I_{mc,\mathrm{ref}}\dfrac{S}{S_{\mathrm{ref}}}(1 + a\Delta T) \\ U_m = U_{mc,\mathrm{ref}}\ln(e + b\Delta S)(1 - c\Delta T) \end{cases} \tag{5}$$

where S is the output power of the PV array; subscript ref denotes the reference value; ΔS is the difference; ΔT is the change in temperature from nominal conditions; a, b and c are parameters available from the manufacturer.

The U_{dc}-I_{PV} characteristic of a PV array can be obtained by extending (2) according to the array dimensions:

$$I_{PV} = N_p I_{sc}\left[1 - C_1\left(\mathrm{e}^{\frac{U_{dc}}{C_2 N_s U_{oc}}} - 1\right)\right] \tag{6}$$

3.2 VSC model and control strategy

Figure 3 shows the topology of the VSC. The mathematical model of VSC is given by (7), which is transformed into a *dq* frame.

$$\begin{cases} L_f\dfrac{\mathrm{d}i_d}{\mathrm{d}t} = U_d - U_{td} + \omega L_f i_q \\ L_f\dfrac{\mathrm{d}i_q}{\mathrm{d}t} = U_q - U_{tq} - \omega L_f i_d \\ U_{dc}C\dfrac{\mathrm{d}U_{dc}}{\mathrm{d}t} = I_{PV}U_{dc} - U_{td}i_d \end{cases} \tag{7}$$

where i_d and i_q are the actual values of the current in the *dq* frame; U_{td} and U_{tq} are the PCC voltages in the *dq* frame; U_d and U_q are the modulation voltages in the *dq* frame.

A typical vector control system for a VSC based on the grid voltage is shown in Fig. 4. The DC voltage U_{dc} and DC current I_{PV} of PV array are sent to the maximum power point tracking (MPPT) controller to generate the DC voltage reference $U_{dc,\mathrm{ref}}$. The outer loop in the *d* frame is the DC voltage controller which produces the current reference $i_{d,\mathrm{ref}}$ for the inner current loop. The outer loop in the *q* frame is the AC-bus voltage controller which produces the current reference $i_{q,\mathrm{ref}}$ for the inner current loop. The inner current controllers produce modulation signals in the

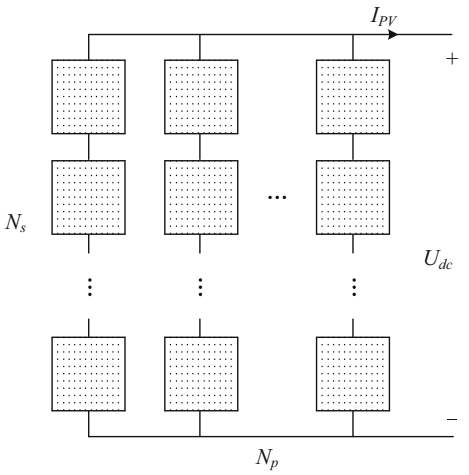

Fig. 2 Configuration of PV array

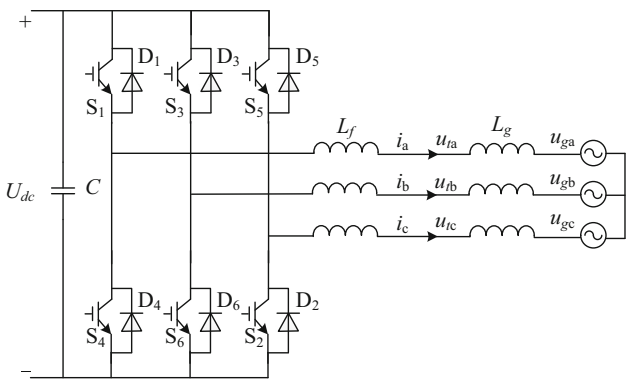

Fig. 3 Topology of VSC

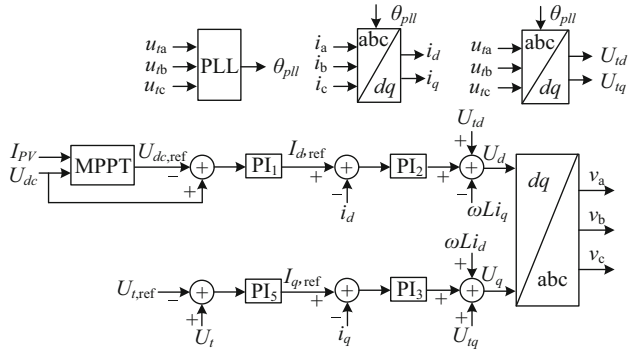

Fig. 4 Control strategy of VSC

dq frame which are then translated back to the abc frame. θ_{pll} is the output phase of the PLL.

According to Fig. 4, the following equations can be obtained:

$$\begin{cases} \dfrac{dx_1}{dt} = U_{dc} - U_{dc,\mathrm{ref}} \\ \dfrac{dx_2}{dt} = k_{p1}(U_{dc} - U_{dc,\mathrm{ref}}) + k_{i1}x_1 - i_d \\ \dfrac{dx_5}{dt} = U_t - U_{t,\mathrm{ref}} \\ \dfrac{dx_3}{dt} = k_{p5}(U_t - U_{t,\mathrm{ref}}) + k_{i5}x_5 - i_q \\ U_d = k_{p2}\left[k_{p1}(U_{dc} - U_{dc,\mathrm{ref}}) + k_{i1}x_1 - i_d\right] + k_{i2}x_2 + U_{td} - \omega L i_q \\ U_q = k_{p3}\left[k_{p5}(U_t - U_{t,\mathrm{ref}}) + k_{i5}x_5 - i_q\right] + k_{i3}x_3 + U_{tq} + \omega L i_d \end{cases} \tag{8}$$

where x_1, x_2, x_3 and x_5 are the state variables; k_{p1}, k_{p2}, k_{p3} and k_{p5} are the proportional gains of the controllers; k_{i1}, k_{i2}, k_{i3} and k_{i5} are the integral gains of the controllers.

Figure 5 shows the working principle of the PLL that is employed to make sure that the *d* frame is always aligned with the PCC voltage phasor $\dot{U}_t$ to synchronize the VSC with the grid. In Fig. 5, $\dot{U}_t'$ is the actual PCC voltage phasor in the *dq* frame. When the PLL is exactly locked, $\dot{U}_t$ and $\dot{U}_t'$ should coincide and the angle θ_{pllx} would then be 0.

The transformation for the PCC voltage and current from the *dq* frame to the *d'q'* frame is given below. Based on the small-angle assumption that $\cos(\theta_{pllx}) = 1$, $\sin(\theta_{pllx}) = \theta_{pllx}$, (10) can be obtained.

$$\begin{cases} U_{td}' = U_{td}\cos(\theta_{pllx}) - U_{tq}\sin(\theta_{pllx}) \\ U_{tq}' = U_{td}\sin(\theta_{pllx}) + U_{tq}\cos(\theta_{pllx}) \\ i_d' = i_d\cos(\theta_{pllx}) - i_q\sin(\theta_{pllx}) \\ i_q' = i_d\sin(\theta_{pllx}) + i_q\cos(\theta_{pllx}) \end{cases} \tag{9}$$

$$\begin{cases} U_{td}' = U_{td} - U_{tq}\theta_{pllx} \\ U_{tq}' = U_{td}\theta_{pllx} + U_{tq} \\ i_d' = i_d - i_q\theta_{pllx} \\ i_q' = i_d\theta_{pllx} + i_q \end{cases} \tag{10}$$

The control strategy of the PLL is shown in Fig. 6 and (11) can be obtained from it.

$$\begin{cases} \dfrac{dx_{pll}}{dt} = U_{tq} \\ \dfrac{d\theta_{pll}}{dt} = k_{p4}U_{tq} + k_{i4}x_{pll} + \omega_0 \end{cases} \tag{11}$$

where x_{pll} is the state variable; k_{p4} and k_{i4} are the PLL parameters.

3.3 Grid model

The equivalent circuit of the AC side of PV generation connected to a weak AC grid is shown in Fig. 7, and the Kirchoff voltage law can be written as:

$$\begin{cases} L_g\dfrac{di_d}{dt} = U_{td} - U_{gd} + \omega L_g i_q \\ L_g\dfrac{di_q}{dt} = U_{tq} - U_{gq} - \omega L_g i_d \end{cases} \tag{12}$$

$$U_{td}' + \mathrm{j}U_{tq}' = U_{gd} + \mathrm{j}U_{gq} + \mathrm{j}(i_d' + \mathrm{j}i_q')x_g \tag{13}$$

Equations (6)–(13) form a set of differential-algebraic equations, which can accurately describe the behaviour of PV generation connected to a weak grid. In order to develop a small-signal model for the system, the equations must first be linearized around the operating point. Following the detailed derivation procedure shown in

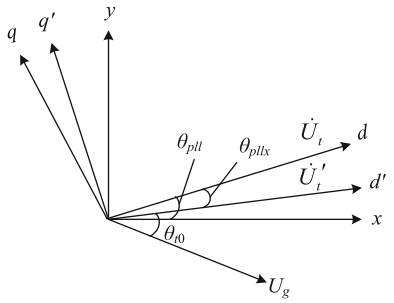

Fig. 5 Working principle of PLL

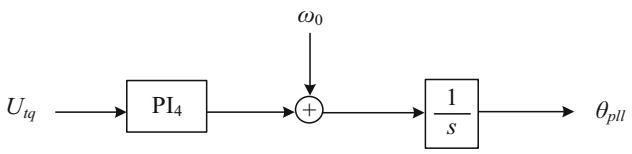

Fig. 6 Control strategy of PLL

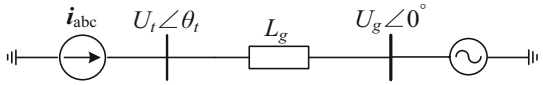

Fig. 7 Equivalent circuit of PV generation connected to AC grid

Appendix A, the small-signal model of the system is expressed in state-space equations as:

$$\Delta\dot{\boldsymbol{x}} = \boldsymbol{A}\Delta\boldsymbol{x} + \boldsymbol{B}\Delta\boldsymbol{u} \tag{14}$$

where $\boldsymbol{A}$ is the state matrix defined in Appendix A; $\boldsymbol{B}$ is the input matrix; $\Delta\boldsymbol{x}$ is the state vectors, which is defined as $\Delta\boldsymbol{x} = [\Delta x_1, \Delta x_2, \Delta x_3, \Delta x_5, \Delta x_{pll}, \Delta\theta_{pll}, \Delta i_d, \Delta i_q, \Delta U_{dc}]^{\mathrm{T}}$.

The eigenvalues of the state matrix $\boldsymbol{A}$ supply useful information about the small-signal stability of the system. The participation factor matrix obtained from the left and right eigenvectors gives insight into the relationship between the states and the modes.

3.4 Model validation

In order to validate the small-signal model, the time-domain response of an example PV array and AC grid was calculated using the small-signal model implemented in MATLAB, and compared with the time-domain response calculated using the full nonlinear model simulated on the electromagnetic transient simulation program PSCAD/EMTDC.

The rated power of the PV array is 500 kW, and the controller parameters of the VSC are listed in Table 1. Under a perturbation of illumination, in which the illumination changes from 800 to 1000 W/m^2 at t = 3 s and from 1000 W/m^2 back to 800 W/m^2 at t = 4.5 s, the operation curves calculated by the two models are compared in Fig. 8a. As can be seen from Fig. 8a, there is a deviation between the curves that depends on the sampling time t_{mppt} of the MPPT controller.

In Fig. 4, the DC voltage reference of the VSC is determined by the MPPT controller. The small-signal model established in this paper does not consider the impact of the maximum power tracking controller, while the simulation model in PSCAD includes the maximum power tracking process. Therefore, when the MPPT has a smaller sampling time, it becomes more responsive and the deviation from the small-signal model becomes larger, as shown in Fig. 8a.

Under a perturbation of impedance perturbation, in which the illumination is constant, while the grid inductance changes from 0.2 mH to 0.25 mH at t = 3 s and from 0.25 mH back to 0.2 mH at t = 4.5 s, the operation curves calculated by the two models ae compared in Fig. 8b. They are basically the same because MPPT has no influence on the system's response to grid impedance.

Table 1 Main parameters

Parameters	Values
The rating power of PV array P	500 kW
Grid voltage U_g	380 V
DC voltage U_{dc}	600 V
Input filter capacitance C	0.02 F
The output filter inductance L_f	0.5 mH
The output filter capacitance C_f	100 μF
Grid inductance L_g	0.6 mH
DC voltage control loop (k_{p1}, k_{i1})	(2, 200)
AC voltage control loop (k_{p5}, k_{i5})	(2, 100)
Active current control loop (k_{p2}, k_{i2})	(2, 100)
Reactive current control loop (k_{p3}, k_{i3})	(2, 100)
PLL (k_{p4}, k_{i4})	(50, 1500)

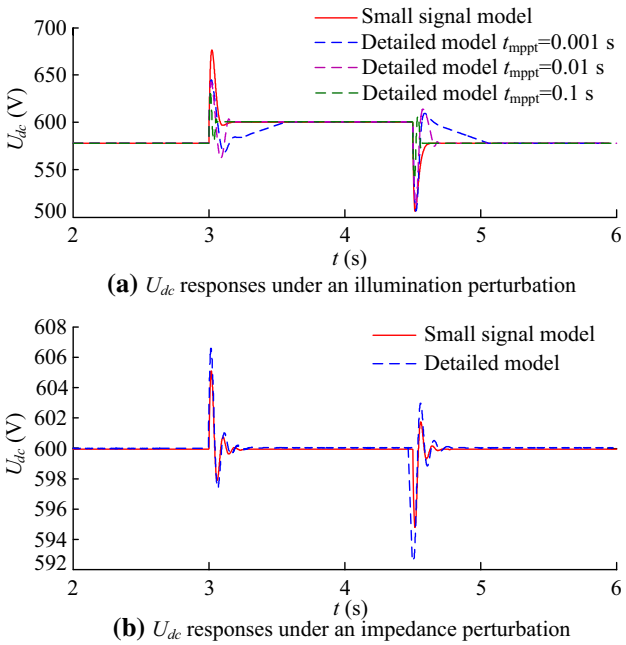

(a) U_{dc} responses under an illumination perturbation

(b) U_{dc} responses under an impedance perturbation

Fig. 8 Validation of the small-signal model

4 Small-signal stability analysis

4.1 Eigenvalue analysis

In order to obtain the eigenvalues, taking the PV generation system shown in Fig. 1 as an example, the system parameters are shown in Table 1 (all of the parameters are expressed per unit with respect to the output side voltage level of the VSC). Table 2 shows all the system modes with frequency and damping of the oscillation, under the condition that the R_{SCR} is equal to 1.5. As can be seen from Table 2, the system has two oscillation modes and five damping modes. All the eigenvalues of the system are distributed on the left side of the complex plane, meaning the system is stable.

Table 2 Eigenvalues of state matrix of a PV system connected to a weak grid

Mode	Eigenvalue	Oscillation frequency (Hz)	Damping
λ_1	− 3885.9	0	1.000
λ_2	− 5455.4	0	1.000
λ_3, λ_4	− 40.1 ± j70.3	11.2	0.495
λ_5, λ_6	− 7.3 ± j28.5	4.5	0.248
λ_7	− 17.8	0	1.000
λ_8	− 50.3	0	1.000
λ_9	− 50.6	0	1.000

Table 3 Participation factors of state variables in nine modes

Variable	Participation factor						
	λ_1	λ_2	λ_3, λ_4	λ_5, λ_6	λ_7	λ_8	λ_9
x_1	0	0	0.57	0.06	0.02	0	0
x_2	0.01	0	0	0	0	1	0
x_3	0	0.01	0	0	0	0	1.00
x_5	0	0	0.02	0.18	0.68	0	0
x_{pll}	0	0	0.07	0.40	0.20	0	0
θ_{pll}	0	0	0.16	0.49	0.08	0	0
i_d	1.00	0	0.01	0	0	0	0
i_q	0	1.00	0	0	0	0	0.01
U_{dc}	0.02	0	0.51	0.06	0.01	0	0

Table 3 shows the participation factors of the state variables in each of the modes identified in Table 2. There are nine modes shown in Table 3. The largest participation of state variables is in modes 3, 4 (λ_3, λ_4) and is associated with the DC voltage control. The PLL is related to modes 5, 6 (λ_5, λ_6).

4.2 Eigenvalues locus analysis

The factors influencing stability of the system include grid strength and different control parameters in the PLL controller. Their influence will be discussed using the small-signal model of PV generation connected to a weak grid.

The system parameters are shown in Table 1. The eigenvalue locus as the R_{SCR} varies from 4 to 1.2 is shown in Fig. 9. As the grid strength decreases, it can be seen that λ_2, λ_3, λ_4 and λ_7 move further to the left, λ_1, λ_8 and λ_9 change little, and λ_5 and λ_6 move towards the right-half plane. When the R_{SCR} reaches 1.2, λ_5 and λ_6 enter the unstable region, and the system becomes unstable.

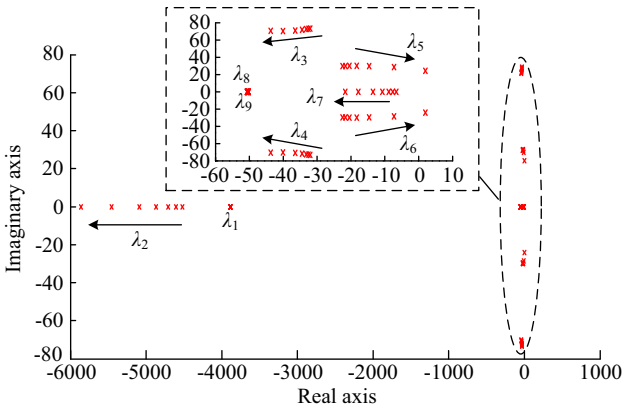

Fig. 9 Eigenvalue locus for varying grid strength

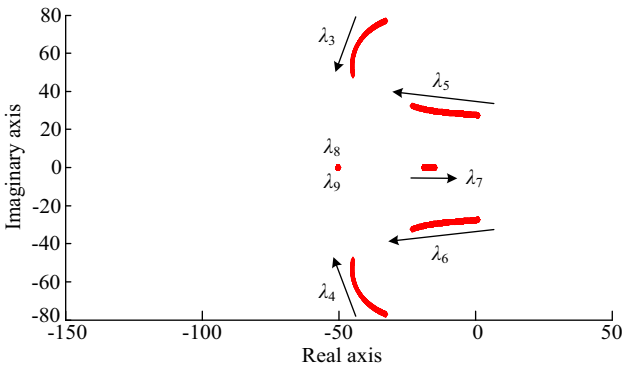

Fig. 10 Eigenvalue locus for varying k_{p4}

Therefore, the stability of PV generation connected to a weak grid becomes worse with the reduction of grid strength.

When the R_{SCR} is fixed at 1.5, the eigenvalue locus as the proportional gain of PLL k_{p4} varies from 10 to 100 is shown in Fig. 10. As k_{p4} increases, it can be seen that λ_3, λ_4, λ_5 and λ_6 move further to the left, while λ_7 moves towards right-half plane. When k_{p4} is 10, λ_5 and λ_6 enter the unstable region, so the system becomes unstable.

When k_{p4} is fixed at 50, the eigenvalue locus as the integral gain of the PLL k_{i4} varies from 100 to 1500 is shown in Fig. 11. As k_{i4} increases, it can be seen that λ_3, λ_4 and λ_7 move further to the left, while λ_5 and λ_6 move towards the right-half plane, but do not enter the unstable region.

In conclusion, the decreasing strength of the grid may cause oscillatory phenomena, tuning the proportional gains of PLL controller have a noticeable effect on the damping characteristics of the system, and larger proportional gain of PLL controller could improve the system damping.

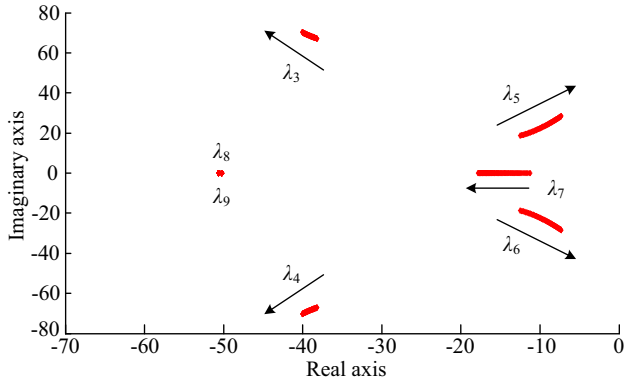

Fig. 11 Eigenvalue locus for varying k_{i4}

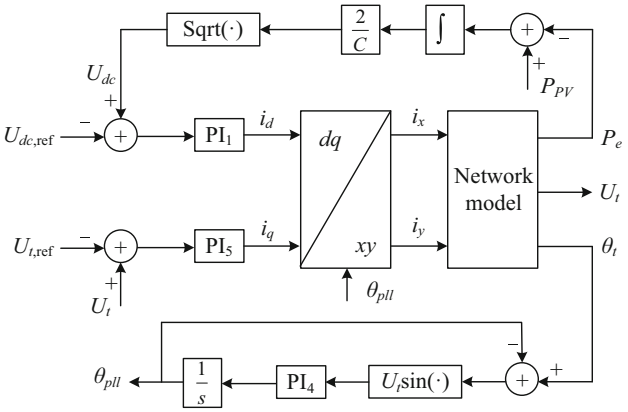

Fig. 12 Simplified power control loop of VSC

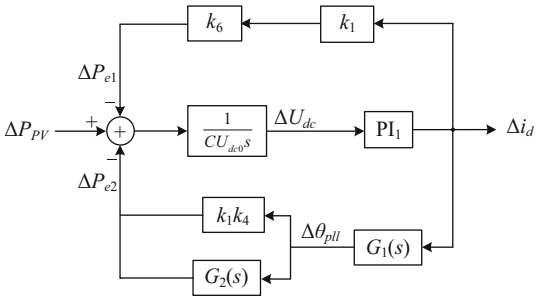

Fig. 13 Further simplified power control loop of VSC

4.3 Transfer function of power control loop in *dq* rotation frame

Based on the eigenvalue analysis above, there is a 4-5 Hz oscillation in the PV generation system when the parameters of PLL controller are not selected properly. To reveal how the PLL control parameters influence the small-signal stability of PV generation, consider that the current control loop bandwidth is much higher than the DC voltage control loop bandwidth. According to the method of [4], the current in the PLL reference frame can track its reference instantaneously ($i_{d,\mathrm{ref}} = i_d$). The VSC and its control system are simplified as shown in Fig. 12, where P_{PV} and P_e are the output powers of the PV array and the VSC, respectively.

The power control loop in Fig. 12 can be further simplified, as shown in Fig. 13 [4]. The transfer functions $G_1(s)$ and $G_2(s)$ are defined as:

$$G_1(s) = \frac{\Delta\theta_{pll}}{\Delta i_d} = \frac{k_6 k_{p4} s + k_6 k_{i4}}{s^2 - k_4 k_{p4} s - k_4 k_{i4}} \tag{15}$$

$$G_2(s) = k_3 k_5 + k_2 \tag{16}$$

where coefficients k_1 to k_6 are given in detail in Appendix B, and they have specific physical meanings which relate to the structure, parameters and operating conditions of the system. k_1 represents the influence of the q-axis terminal voltage variation on the output active power; k_2, k_4 and k_5 represent the influence of the output of the PLL variation on the output active power, the q-axis terminal voltage and the d-axis terminal voltage, respectively; k_3 represents the influence of the d-axis terminal voltage variation on the output active power; and k_6 represents the influence of the d-axis current variation on the q-axis terminal voltage.

In Fig. 13, the transfer functions $G_s(s)$ and $G_m(s)$ are defined as:

$$G_s(s) = k_1 k_6 \tag{17}$$

$$G_m(s) = G_1(s)(k_1 k_4 + G_2(s)) \tag{18}$$

According to (15)–(18), the open loop transfer function $G_o(s)$ can be obtained as:

$$G_o(s) = \frac{\Delta P_e}{\Delta P_{PV}} = (G_m(s) + G_s(s))\left(k_{p1} + \frac{k_{i1}}{s}\right)\frac{1}{CU_{dc0}s} \tag{19}$$

By neglecting the effect of the PLL controller dynamics, the Bode diagram of $G_o(s)$ is shown in Fig. 14. It shows that, with decreasing grid strength, the phase margin of $G_o(s)$ decreases and the stability of the system becomes weaker.

Considering the effect of the PLL controller dynamics ($R_{\mathrm{SCR}} = 1.5$), the Bode diagrams of $G_s(s)$, $G_m(s)$ and $G_o(s)$ are shown in Figs. 15 and 16, respectively. As can be seen from Fig. 15, when the proportional gain of the PLL k_{p4} becomes 10 and the integral gain of PLL k_{i4} becomes 1500, the amplitude of $G_m(s)$ is greater than the amplitude of $G_s(s)$ in the frequency range of 4-5 Hz, and the phase of $G_m(s)$ is approximately equal to 180°. Within the frequency range of 4-5 Hz, the PLL controller has positive feedback on the power loop of PV generation. As can be seen from Fig. 16, with decreasing PLL control parameters, the phase margin of $G_o(s)$ also decreases. The results of the above

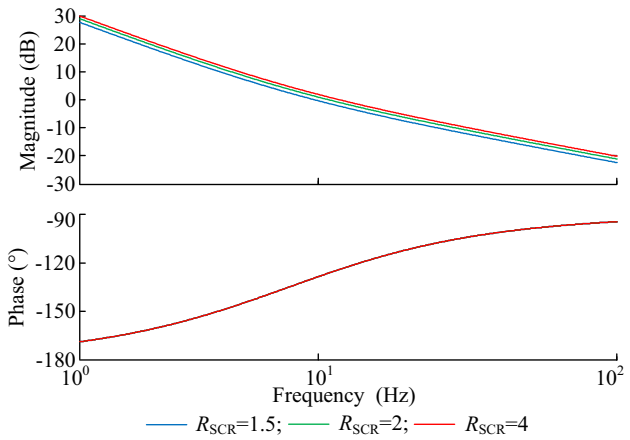

Fig. 14 Bode diagram of $G_o(s)$ by neglecting effect of PLL controller dynamics

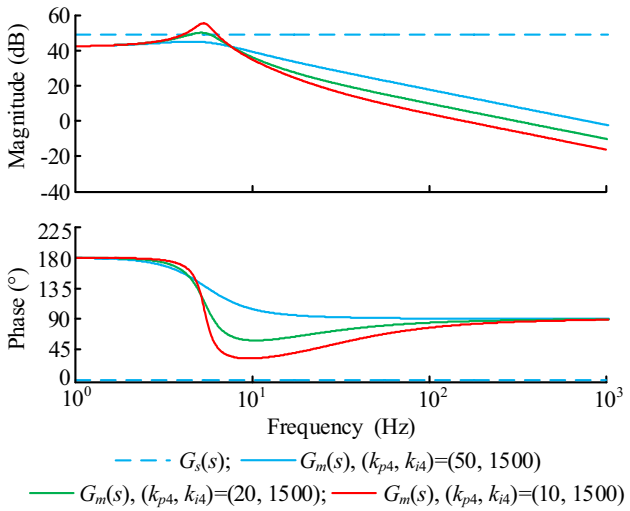

Fig. 15 Bode diagrams of $G_s(s)$ and $G_m(s)$

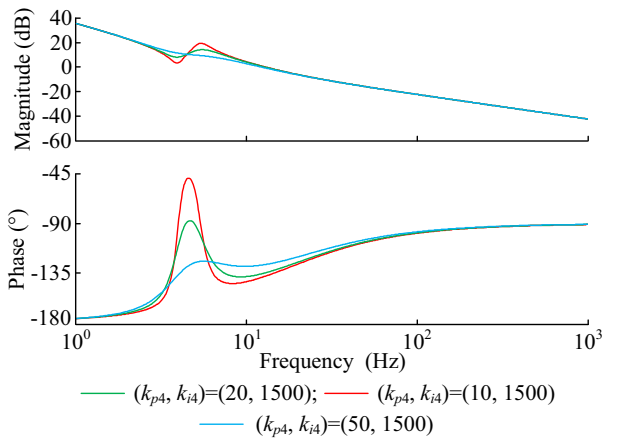

Fig. 16 Bode diagram of $G_o(s)$

analysis are consistent with the results of the eigenvalues analysis.

5 Virtual inductance control strategy

According to the eigenvalue analysis, we can see that changing the controller parameters can improve the operational stability of PV generation. However, the control loop interactions become obvious under weak AC grid conditions, meaning the parameters should be designed together and existing optimization methods may not be applicable to design them. Therefore, a new simple method involving a virtual inductance control strategy is proposed in this paper, which is equivalent to developing a virtual PCC voltage for VSC synchronization in the control system. The corresponding equivalent circuit is shown in Fig. 17. The relationship between the virtual PCC voltage $\boldsymbol{U}_{tdq,\mathrm{vir}}$ and the PCC voltage $\boldsymbol{U}_{tdq}$ is given in (20), and $\boldsymbol{U}_{tdq,\mathrm{vir}}$ will be sent to the control system to modify the input value of PLL controller as shown in Fig. 18.

$$\begin{cases} U_{td,\mathrm{vir}} = U_{td} + \omega_{pll} L_{\mathrm{vir}} i_q \\ U_{tq,\mathrm{vir}} = U_{tq} - \omega_{pll} L_{\mathrm{vir}} i_d \\ L_{\mathrm{vir}} = aL_g \end{cases} \tag{20}$$

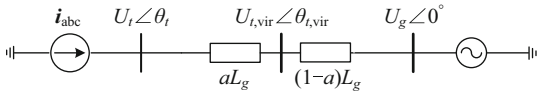

Fig. 17 Equivalent circuit of PV generation connected to the AC grid with a virtual PCC voltage

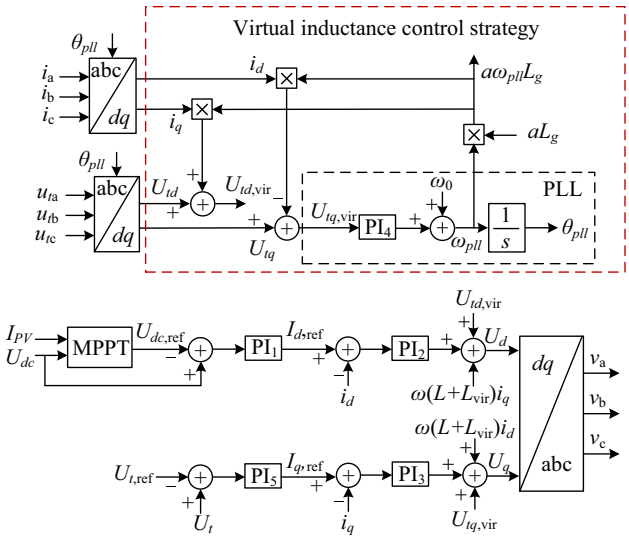

Fig. 18 Modified control strategy of VSC

where a is the virtual control coefficient, $0 \le a \le 1$.

In order to explain the influence of the virtual inductance control strategy on the operation stability of PV generation further, $\boldsymbol{U}_{tdq,\mathrm{vir}}$ is introduced to (14) to modify the small-signal model. Comparing with the original matrix $\boldsymbol{A}$, the four elements $A_{57} = x_g$, $A_{67} = k_{p4}x_g$, $A_{78} = 0$, $A_{87} = 0$ would change to $A_{57} = (1-a)x_g$, $A_{67} = k_{p4}(1-a)x_g$, $A_{78} = ax_g/L$, $A_{87} = -ax_g/L$. When a is 0.5, the eigenvalue locus as the R_{SCR} varies from 4 to 1.2 is shown in Fig. 19, and the eigenvalue locus as the proportional gain of the PLL k_{p4} varies from 10 to 100 is shown in Fig. 20. The red eigenvalue locus represents PV generation with the virtual inductance control strategy and the blue eigenvalue locus represents PV generation without the virtual inductance control strategy. Figures 19 and 20 show that the PV generation becomes stable with the virtual inductance control strategy.

When VSC adopts the virtual inductance control strategy, the transfer functions $G_1(s)$ and $G_m(s)$ in Section 4 should be modified. $G_1(s)$ and $G_m(s)$ are depicted in (21) and (22) (according to Appendix B, $k_6 = x_g$). When the R_{SCR} turns is 1.5, the proportional gain of PLL k_{p4} is 10 and the integral gain of PLL k_{i4} is 1500, the Bode diagram of $G_m(s)$ with different virtual control coefficients a is shown in Fig. 21. It shows that, when the virtual control coefficient a increases, the amplitude of $G_m(s)$ will be lower than the amplitude of $G_s(s)$ in the frequency range of 4-5 Hz. Compared with the results shown in Fig. 15, the PV generation will become stable when employing a virtual inductance control strategy, and the results of the above analysis are consistent with the eigenvalues analysis.

$$G_1(s) = \frac{\Delta\theta_{pll}}{\Delta i_d} = \frac{(k_6 - ax_g)k_{p4}s + (k_6 - ax_g)k_{i4}}{s^2 - k_4k_{p4}s - k_4k_{i4}} \tag{21}$$

$$G_m(s) = \frac{(1-a)x_gk_{p4}s + (1-a)x_gk_{i4}}{s^2 - k_4k_{p4}s - k_4k_{i4}}(k_1k_4 + G_2(s)) \tag{22}$$

6 Simulation validation

In order to verify the effectiveness of the small-signal analysis, a detailed simulation model of PV generation connected to a weak AC grid is built in PSCAD/EMTDC. The parameters are shown in Table 1.

6.1 Simulation results and analysis

When the proportional gain of PLL k_{p4} is 50, and the integral gain of PLL is 1500, Figs. 22 and 23 show the PCC voltage U_t responses, DC voltage U_{dc} responses, output active power P_e responses and d-axis current i_d responses calculated by the detailed simulation model for a step change of illumination at $t = 10$ s with different grid strengths.

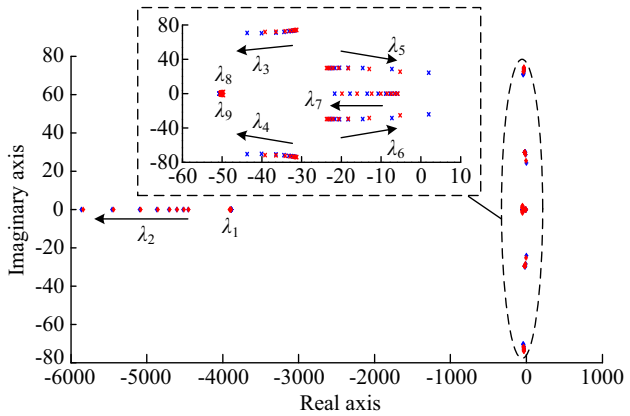

Fig. 19 Eigenvalue locus for varying grid strength ($a = 0.5$)

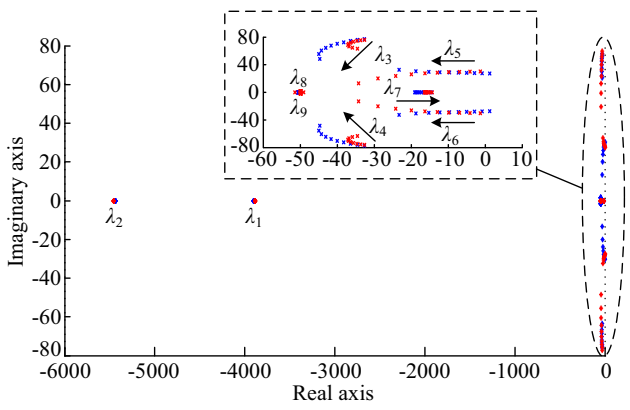

Fig. 20 Eigenvalue locus for varying k_{p4} ($a = 0.5$)

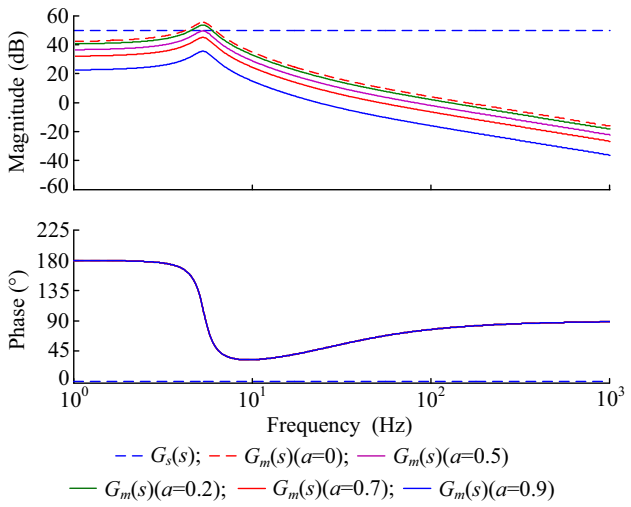

Fig. 21 Bode diagrams of $G_s(s)$ and $G_m(s)$ with different a

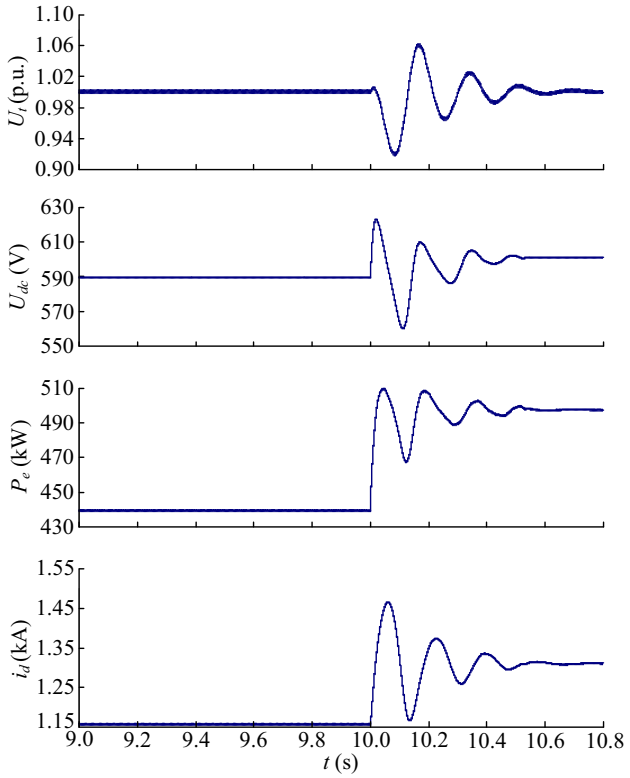

Fig. 22 Stable waveforms when R_{SCR} is 1.5

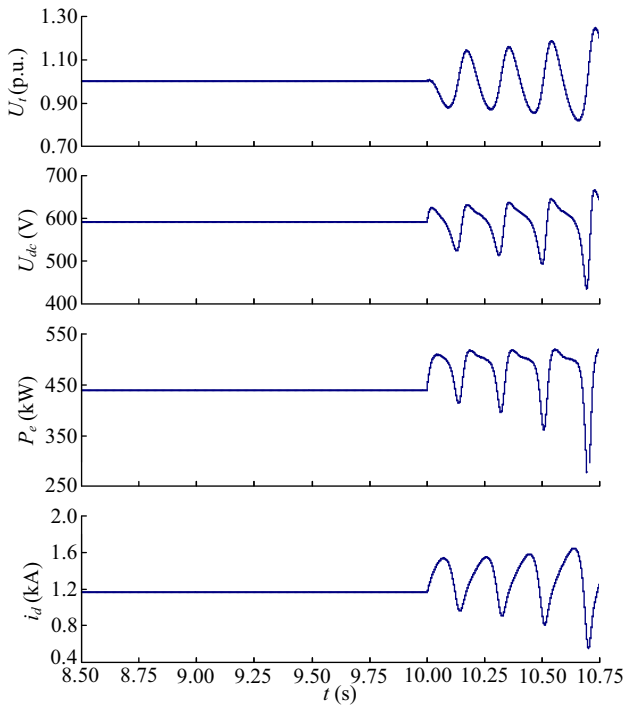

Fig. 23 Unstable waveforms when R_{SCR} is 1.2

Figure 22 illustrates that the system becomes stable after a step change of illumination when R_{SCR} = 1.5. Figure 23 illustrates that the system becomes unstable after a step change of illumination when R_{SCR} = 1.2.

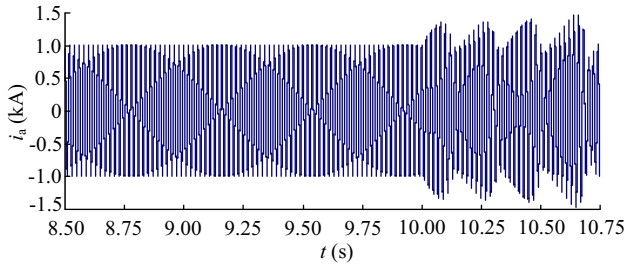

Fig. 24 Current i_a responses when R_{SCR} is 1.2

Table 4 Oscillation modes of i_a in Fig. 24 (to 18th order)

Mode	Amplitude	Frequency (Hz)	Damping
1, 2	1100.000	5	− 0.08
3	120.000	0	− 130.00
4, 5	2.700	340	− 670.00
6, 7	0.440	810	− 1500.00
8, 9	0.088	1300	− 2000.00
10, 11	0.070	1900	− 2400.00
12, 13	0.032	2900	− 3300.00
14	0.029	4200	− 5200.00
15, 16	0.028	3500	− 3700.00
17, 18	0.009	2400	− 2800.00

Figure 24 shows the current i_a responses when R_{SCR} = 1.2. In order to judge the effectiveness of the simulation results, a Prony toolbox is employed using the MATLAB environment to fit the unstable part of i_a (to 18th-order terms). The amplitude, frequency, and damping ratio resulting from the Prony approximate curve are listed in Table 4. It can be seen that the main oscillation frequency is about 5 Hz, which is consistent with the eigenvalue locus analysis in Fig. 9.

When the R_{SCR} is 1.5, Figs. 25 and 26 show the PCC voltage U_t responses, DC voltage U_{dc} responses, output active power P_e responses and d-axis current i_d responses calculated by the detailed simulation model for a step change of illumination at t = 10 s with different PLL gains. In Fig. 25, k_{p4} = 100, k_{i4} = 1500 and in Fig. 26, k_{p4} = 18, k_{i4} = 1500.

Figure 25 illustrates that the system becomes stable after a step change of illumination. Figure 26 illustrates that the system becomes unstable after a step change of illumination.

Figure 27 shows the current i_a responses when k_{p4} = 18. As above, a Prony Toolbox employed to fit the unstable part of i_a (to 18th-order terms). The amplitude, frequency, and damping ratio resulting from the Prony approximate curve are listed in Table 5. It can be seen from

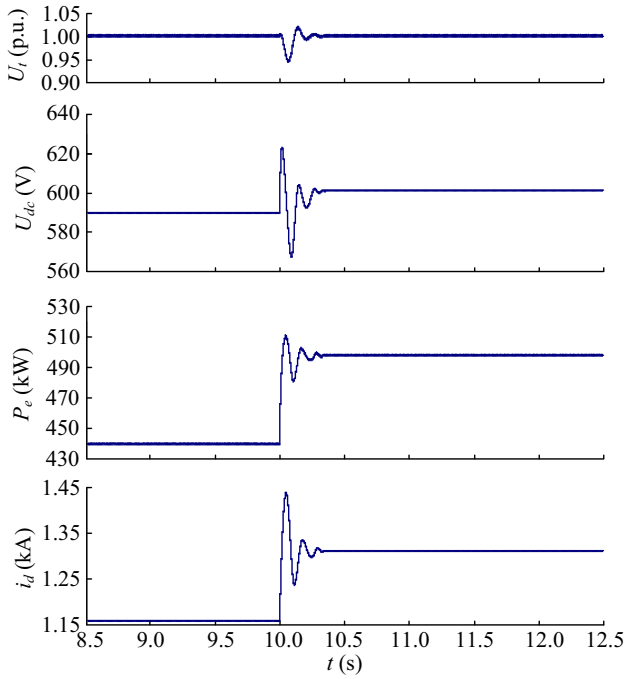

Fig. 25 Stable waveforms when k_{p4} is 100

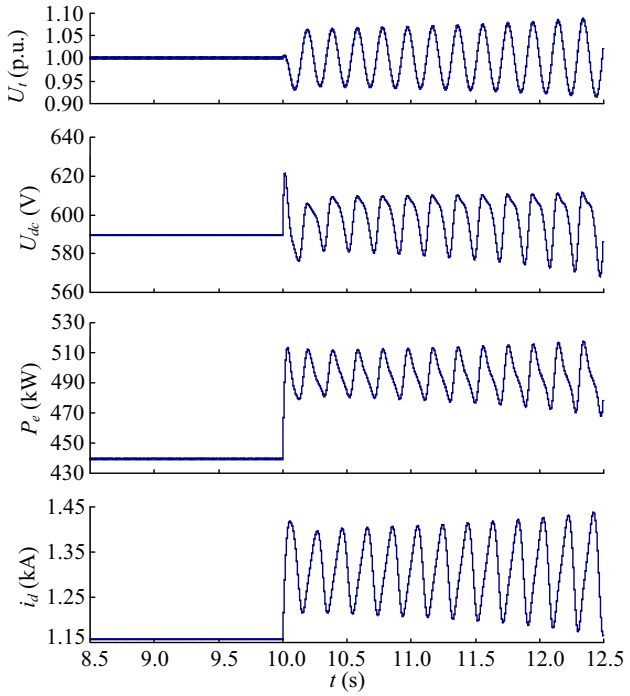

Fig. 26 Unstable waveforms when k_{p4} is 18

Table 5 that the main oscillation frequency is also about 5 Hz, which is consistent with the eigenvalue locus analysis in Fig. 10.

When the R_{SCR} is 1.2 and the virtual control coefficient a turns is 0.5, Fig. 28 shows that the PV generation becomes stable with the virtual inductance control strategy, compared with the instability shown in Fig. 23.

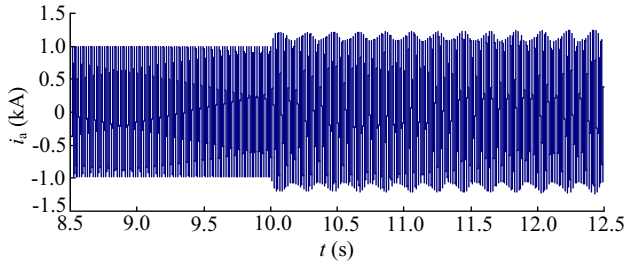

Fig. 27 Current i_a responses when k_{p4} is 18

Table 5 Oscillation modes of i_a in Fig. 27 (to 18th order)

Mode	Amplitude	Frequency (Hz)	Damping
1, 2	1100.0000	5	− 0.022
3	420.0000	0	− 340.000
4	230.0000	0	− 580.000
5, 6	0.4200	340	− 100.000
7, 8	0.1800	630	− 250.000
9, 10	0.0450	940	− 350.000
11, 12	0.0130	1300	− 430.000
13, 14	0.0110	1600	− 500.000
15, 16	0.0045	2300	− 680.000
17, 18	0.0015	1900	− 570.000

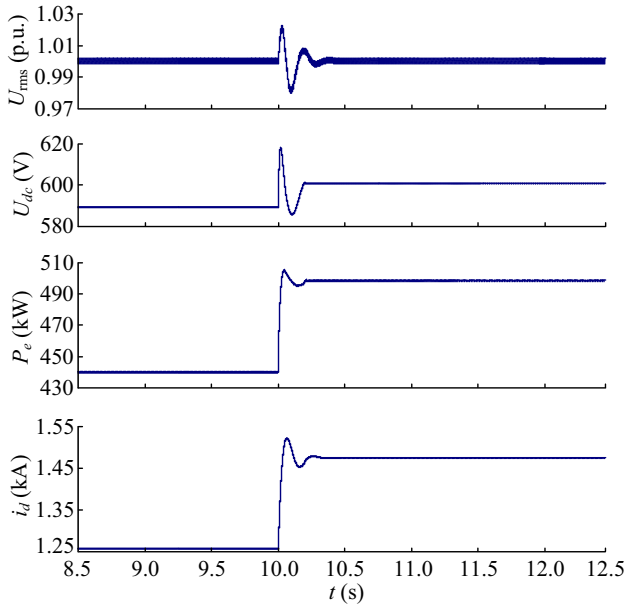

Fig. 28 Stable waveforms when R_{SCR} is 1.2 and virtual control coefficient a is 0.5

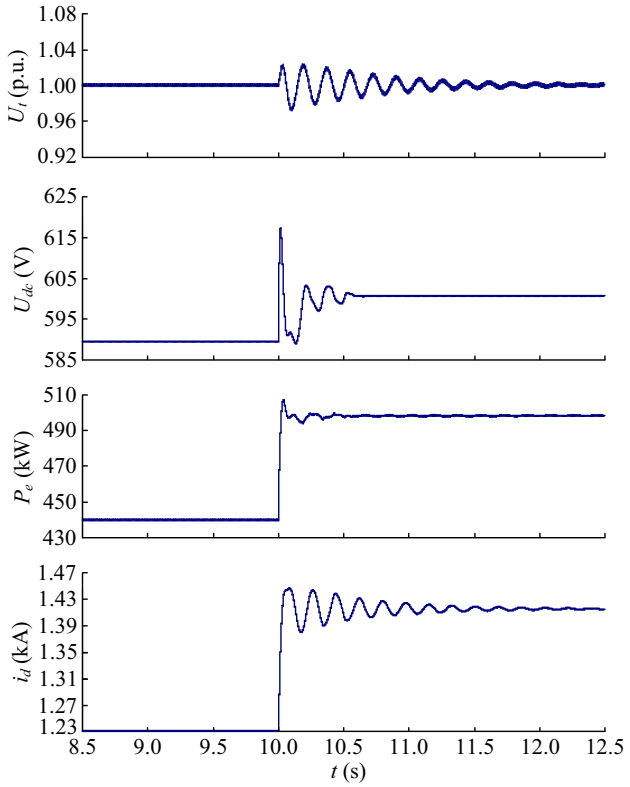

Fig. 29 Stable waveforms when k_{p4} is 10 and virtual control coefficient a is 0.5

When the proportional gain of the PLL k_{p41} is 10 and the virtual control coefficient a is 0.5, Fig. 29 shows that the PV generation becomes stable with the virtual inductance control strategy, compared with the instability shown in Fig. 26. These simulation results are consistent with the eigenvalue locus analysis in Fig. 19 and in Fig. 20.

7 Conclusion

A small-signal model of PV generation connected to a weak grid is presented in this paper. Eigenvalue analysis and the transfer function of the power control loop analyzed in dq rotation frame are employed to study the stability of PV generation with different grid strength and different control parameters in the PLL controller.

The following conclusions can be drawn for the example system parameters used: ① increased output power of a PV unit in a PV generator or decreased grid strength may lead to oscillatory phenomena ($R_{\mathrm{SCR}} \leq 1.2$); ② tuning the gains of the PLL in the VSC has a noticeable effect on the damping characteristic of the system, and larger proportional gain of PLL controller (18-100) can improve system damping and enhance the system stability; ③ within the frequency range of 4-5 Hz, the PLL controller has a positive feedback on the power control loop of PV generation.

In order to improve the operation stability of PV generation, the virtual inductance control strategy is presented in this paper. By selecting a proper virtual control coefficient, the virtual inductance control strategy can improve the operational stability of PV generation. The influence of the grid resistance R_g and the MPPT controller on the system stability will be considered in future work.

Acknowledgements This work was supported by State Grid Corporation of China "Study on active frequency and voltage control technologies for second level power disturbance in photovoltaic power plant" and National Natural Science Foundation of China (No. 51277024).

Appendix A

Linearizing (6)–(8) around the operating point leads to (A1) and (A2):

$$\begin{cases} \dfrac{\mathrm{d}\Delta x_1}{\mathrm{d}t} = \Delta U_{dc} - \Delta U_{dc,\mathrm{ref}} \\ \dfrac{\mathrm{d}\Delta x_2}{\mathrm{d}t} = k_{p1}\Delta U_{dc} + k_{i1}\Delta x_1 - \Delta i_d \\ \dfrac{\mathrm{d}\Delta x_3}{\mathrm{d}t} = k_{p5}\Delta U_t + k_{i5}\Delta x_5 - \Delta i_q \\ \dfrac{\mathrm{d}\Delta x_5}{\mathrm{d}t} = \Delta U_t \\ \dfrac{\mathrm{d}\Delta x_{pll}}{\mathrm{d}t} = \Delta U_{tq} \\ \dfrac{\mathrm{d}\Delta \theta_{pll}}{\mathrm{d}t} = k_{p4}\Delta U_{tq} + k_{i4}\Delta x_{pll} \\ L_f \dfrac{\mathrm{d}\Delta i_d}{\mathrm{d}t} = \Delta U_d - \Delta U_{td} + \omega L_f \Delta i_q \\ L_f \dfrac{\mathrm{d}\Delta i_q}{\mathrm{d}t} = \Delta U_q - \Delta U_{tq} - \omega L_f \Delta i_d \\ C\dfrac{\mathrm{d}\Delta U_{dc}}{\mathrm{d}t} = \Delta i_{PV} + \dfrac{i_{PV0}}{U_{dc0}}\Delta U_{dc} - \dfrac{U_{td0}}{U_{dc0}}\Delta i_d - \dfrac{i_{d0}}{U_{dc0}}\Delta U_{td} \end{cases} \tag{A1}$$

$$\begin{cases} \Delta U_d = k_{p2}k_{p1}(\Delta U_{dc} - \Delta U_{dc,\mathrm{ref}}) + k_{p2}k_{i1}\Delta x_1 \\ \qquad -k_{p2}\Delta i_d + k_{i2}\Delta x_2 + \Delta U_{td} - \omega L_f \Delta i_q \\ \Delta U_q = k_{p3}k_{p5}(\Delta U_t - \Delta U_{t,\mathrm{ref}}) + k_{p3}k_{i5}\Delta x_5 \\ \qquad -k_{p3}\Delta i_q + k_{i3}\Delta x_3 + \Delta U_{tq} + \omega L_f \Delta i_d \end{cases} \tag{A2}$$

Linearizing (10) around the operating point leads to (A3):

$$\begin{cases} \Delta U'_{td} = \Delta U_{td} - U_{tq0}\Delta\theta_{pll} \\ \Delta U'_{tq} = U_{td0}\Delta\theta_{pll} + \Delta U_{tq} \\ \Delta i'_d = \Delta i_d - i_{q0}\Delta\theta_{pll} \\ \Delta i'_q = i_{d0}\Delta\theta_{pll} + \Delta i_q \end{cases} \tag{A3}$$

Linearizing (13) around the operating point leads to (A4):

$$\begin{cases} \Delta U'_{td} = -\Delta i'_q x_g \\ \Delta U'_{tq} = \Delta i'_d x_g \end{cases} \tag{A4}$$

Combining (A3) and (A4) gives:

$$\begin{cases} \Delta U_{td} = -x_g\Delta i_q + (U_{tq0} - i_{d0}x_g)\Delta\theta_{pll} \\ \Delta U_{tq} = x_g\Delta i_d - (U_{td0} + i_{q0}x_g)\Delta\theta_{pll} \end{cases} \tag{A5}$$

Substituting (A2) and (A5) into (A1) leads to (14) in Section 3. The state matrix is as (A6).

$$\boldsymbol{A} = \begin{bmatrix} 0 & 0 & 0 & 0 & 0 & 0 & 0 & 0 & 1 \\ k_{i1} & 0 & 0 & 0 & 0 & 0 & -1 & 0 & k_{p1} \\ 0 & 0 & 0 & k_{i5} & 0 & k_{p5}(U_{tq0} - i_{d0}x_g) & 0 & -(1 + k_{p5}x_g) & 0 \\ 0 & 0 & 0 & 0 & 0 & (U_{tq0} - i_{d0}x_g) & 0 & -x_g & 0 \\ 0 & 0 & 0 & 0 & 0 & -(U_{td0} + i_{q0}x_g) & x_g & 0 & 0 \\ 0 & 0 & 0 & 0 & k_{i4} & -k_{p4}(U_{td0} + i_{q0}x_g) & k_{p4}x_g & 0 & 0 \\ \dfrac{k_{p2}k_{i1}}{L_f} & \dfrac{k_{i2}}{L_f} & 0 & 0 & 0 & 0 & -\dfrac{k_{p2}}{L_f} & 0 & \dfrac{k_{p1}k_{p2}}{L_f} \\ 0 & 0 & \dfrac{k_{i3}}{L_f} & \dfrac{k_{p3}k_{i5}}{L_f} & 0 & \dfrac{k_{p3}k_{p5}(U_{tq0} - i_{d0}x_g)}{L_f} & 0 & -\dfrac{k_{p3}k_{p5}x_g + k_{p3}}{L_f} & 0 \\ 0 & 0 & 0 & 0 & 0 & t_1 & t_2 & t_3 & t_4 \end{bmatrix} \tag{A6}$$

$$\begin{cases} t_1 = -\dfrac{i_{d0}}{CU_{dc0}}(U_{tq0} - i_{d0}x_g) \\ t_2 = -\dfrac{U_{td0}}{CU_{dc0}} \\ t_3 = \dfrac{i_{d0}}{CU_{dc0}}x_g \\ t_4 = \dfrac{1}{C}\left(\alpha + \dfrac{i_{PV0}}{U_{dc0}}\right) \end{cases} \tag{A7}$$

Appendix B

According to [4], the following equations can be obtained:

$$\begin{cases} \Delta P_e = k_1\Delta U_{tq} + k_2\Delta\theta_{pll} + k_3\Delta U_{td} \\ \Delta U_{tq} = k_4\Delta\theta_{pll} + k_6\Delta i_d \\ \Delta U_{td} = k_5\Delta\theta_{pll} + k_7\Delta i_q \\ \Delta U_t = \Delta U_{td} \end{cases} \tag{B1}$$

$$\begin{cases} k_1 = U_{gd0}/x_g \\ k_2 = U_{gd0}U_{td0}/x_g \\ k_3 = -U_{gq0}/x_g \\ k_4 = -i_{q0}x_g - U_{td0} \\ k_5 = -i_{d0}x_g \\ k_6 = x_g \\ k_7 = -x_g \end{cases} \tag{B2}$$

References

[1] Yang ST, Lei Q, Peng FZ et al (2011) A robust control scheme for grid-connected voltage-source inverters. IEEE Trans Ind Electron 58(1):202–212

[2] Zhou L, Zhang M, Ju XL et al (2013) Stability analysis of large-scale photovoltaic power plants for the effect of grid impedance. Proc CSEE 33(34):34–41

[3] Hu J, Huang Y, Wang D et al (2015) Modeling of grid-connected DFIG-based wind turbines for DC-link voltage stability analysis. IEEE Trans Sustain Energy 6(4):1325–1335

[4] Huang Y, Yuan X, Hu J et al (2015) Modeling of VSC connected to weak grid for stability analysis of DC-link voltage control. IEEE J Emerg Sel Top Power Electron 3(4):1193–1204

[5] Hernandez JC, Bueno PG, Sanchez-Sutil F (2017) Enhanced utility-scale photovoltaic units with frequency support functions and dynamic grid support for transmission systems. IET Renew Power Gener 11(3):361–372

[6] Bueno PG, Hernandez JC, Ruiz-Rodriguez FJ (2016) Stability assessment for transmission systems with large utility-scale photovoltaic units. IET Renew Power Gener 10(5):584–597

[7] Jian S (2011) Impedance-based stability criterion for grid-connected inverters. IEEE Trans Power Electron 26(11):3075–3078

[8] Jian S (2009) Small-signal methods for AC distributed power systems—a review. IEEE Trans Power Electron 24(11):2545–2554

[9] Liserre M, Teodorescu R, Blaabjerg F (2004) Stability of grid-connected PV inverters with large grid impedance variation. In: Proceedings of 2004 IEEE 35th annual power electron specialists conference, Aachen, Germany, 20–25 June 2004, pp 4773–4779

[10] Juan LA, Mikel B, Jesus L et al (2011) Modeling and control of *N*-paralleled grid-connected inverters with LCL filter coupled due to grid impedance in PV plants. IEEE Trans Power Electron 26(3):770–785

STATE GRID
STATE GRID ELECTRIC POWER RESEARCH INSTITUTE

[11] Yan G, Ren J, Mu G et al (2016) DC-link voltage stability analysis for single-stage photovoltaic VSIs connected to weak grid. In: Proceedings of 2016 IEEE 8th international power electron and motion control conference, Hefei, China, 22–26 May 2016, pp 474–478
[12] Huang Y, Yuan X, Hu J et al (2016) DC-bus voltage control stability affected by AC-bus voltage control in VSCs connected to weak AC grid. IEEE J Emerg Sel Top Power Electron 4(2):445–458
[13] Zhou P, Yuan XM, Hu JB et al (2014) Stability analysis of DC-link voltage as affected by phase locked loop in VSC when attached to weak grid. In: Proceedings of 2014 IEEE PES general meeting, National Harbor, USA, 27–31 July 2014, pp 474–478
[14] Zhou JZ, Ding H, Fan S et al (2014) Impact of short-circuit ratio and phase-locked-loop parameters on the small-signal behavior of a VSC-HVDC converter. IEEE Trans Power Del 29(5):2287–2296
[15] Nicholas PWS, Dragan J (2010) Stability of a variable-speed permanent magnet wind generator with weak AC grids. IEEE Trans Power Del 25(4):2779–2788
[16] Arani MFM, Mohamed ARI (2017) Analysis and performance enhancement of vector-controlled VSC in HVDC links connected to very weak grids. IEEE Trans Power Syst 32(1):684–693

Qi JIA received the B.S. degree and M.S. degree from Northeast Electric Power University, Jilin, China, where he is currently pursuing the Ph.D. degree in the Electrical Engineering Department. His current research interests include renewable energy generation, stability analysis and control of grid-connected renewable generation.

Gangui YAN received the Ph.D. degree from Tsinghua University in 2003. He is a professor and Ph.D. supervisor at Northeast Electric Power University. His current research interests include renewable energy system, energy storage system and power electronic technique, stability analysis and control of grid-connected renewable generations.

Yuru CAI received the B.S. degree in 2014 from Northeast Electric Power University, Jilin, China, where she is currently pursuing the M.S. degree in the Electrical Engineering Department. Her current research interests include renewable energy generation, stability analysis and control of grid-connected renewable generation.

Yonglin LI received the B.S. degree in 2014 from Northeast Electric Power University, Jilin, China, where he is currently pursuing the M.S. degree in the Electrical Engineering Department. His current research interests include renewable energy generation.

Jinhao ZHANG received the B.S. degree in 2014 from Northeast Electric Power University, Jilin, China, where he is currently pursuing the M.S. degree in the Electrical Engineering Department. His current research interests include renewable energy.